

Wang, H., Byrne, J., Perez, J., Thomas, A., Göttlicher, J., Höfer, H., Mayanna, S., Kontny, A., Kappler, A., Guo, H., Benning, L. G., Norra, S. (2020): Arsenic sequestration in pyrite and greigite in the buried peat of As-contaminated aquifers. - *Geochimica et Cosmochimica Acta*, 284, 107-119.

<https://doi.org/10.1016/j.gca.2020.06.021>

1 **Arsenic sequestration in pyrite and greigite in the buried peat of As-contaminated aquifers**

2 H.Y. Wang^{a*}, J.M. Byrne^b, J.P.H. Perez^{c,d}, A.N. Thomas^a, J. Göttlicher^e, H.E. Höfer^f, S. Mayanna^c,
3 A. Kontny^a, A. Kappler^b, H.M. Guo^g, L.G. Benning^{c,d}, S. Norra^a

4 ^aInstitute of Applied Geoscience, Working Group of Environmental Mineralogy and
5 Environmental System Analysis, Karlsruhe Institute of Technology (KIT), 76131 Karlsruhe,
6 Germany

7 ^bGeomicrobiology, Center for Applied Geosciences, University of Tuebingen, 72074 Tuebingen,
8 Germany

9 ^cGFZ German Research Center for Geoscience, 14473 Potsdam, Germany

10 ^dDepartment of Earth Sciences, Freie Universität Berlin, 12249 Berlin, Germany

11 ^eInstitute of Synchrotron Radiation, Karlsruhe Institute of Technology (KIT), 76131 Karlsruhe,
12 Germany

13 ^fInstitute of Geoscience, Goethe University, 60438 Frankfurt, Germany

14 ^gState key Laboratory of Biogeology and Environmental Geology, China University of Geoscience,
15 100083 Beijing, China

16

17 **Abstract**

18 Detrital peat (organic carbon-enriched deposit) with high arsenic (As) content is widely distributed
19 in sediments where groundwater As contamination exists. Iron sulfides often persist in these
20 sediments under anoxic conditions. However, the mechanisms and pathways of formation of iron
21 sulfides and its potential contribution in controlling As mobility are still poorly understood. In this
22 study, we examined three As-contaminated peat sediments from the Hetao Basin in China to gain
23 better understanding of the complex interplay between iron sulfides formation and As mobility.
24 We employed high-resolution spectroscopic techniques, including X-ray absorption spectroscopy
25 and ^{57}Fe Mössbauer spectroscopy, coupled with electron microscopy to determine the speciation
26 of iron sulfides and the associated As in the peat sediments.

27 Pyrite (FeS_2) and metastable greigite (Fe_3S_4) persisted in peat as end-members of S and Fe
28 diagenetic pathways. The Fe-rich phyllosilicates and decaying plant tissues provided the ideal
29 micro-environments for pyrite and greigite nucleation. Pyrite formation most likely occurred via
30 the polysulfides pathway in the surface water-sediments interface during early diagenetic process,
31 while the relative enrichment of reactive Fe compared to sulfide possibly inhibited the
32 transformation of greigite to pyrite in such Fe-rich sediments.

33 Our results revealed that the peat sediments could act as a stable sink for As immobilization under
34 steady groundwater anoxic conditions, with As content up to 250 mg/kg and large proportions (40
35 to 60 wt.% As) sequestered in pyrite and greigite. Pyrite crystallites had up to 1 wt.% As content
36 through the replacement of the S^{-1} sites. Greigite crystallites had a relatively constant As content
37 ranging from ~500 to ~1,400 mg/kg. Instead of being adsorbed or structurally incorporated, arsenic
38 formed distinct arsenic sulfide phase in the greigite-enriched sediments, which was analogous to
39 realgar. The transfer of As from iron sulfides to ferrihydrite temporarily retarded As release into

40 groundwater under slightly oxic groundwater conditions. However, the reductive dissolution of
41 ferrihydrite and potential subsequent As re-release could be a source of As in groundwater under
42 disturbed redox conditions.

43 **Keywords:** peat; arsenic; greigite; pyrite; sediment biogeochemistry; early diagenesis

44 **Introduction**

45 Over a hundred million people are exposed to groundwater with high levels of arsenic (As) (> 10
46 $\mu\text{g/L}$) globally, particularly in South and Southeast Asia including the Ganges-Brahmaputra-
47 Megha, Red River and Mekong Deltas and the basins belong to the Yangtze and Yellow River
48 catchments (Winkel et al., 2008; Fendorf et al., 2010; Wang et al., 2019 b). It is widely accepted
49 that microbial reduction of Fe (oxyhydr)oxides coupled to organic carbon oxidation causes the
50 release of Fe (oxyhydr)oxides-bound As into groundwater (Nickson et al., 1998; Islam et al., 2004;
51 Guo et al., 2013). The reactivity and availability of organic matter, partitioning of As in solids and
52 the presence of other redox-active species (e.g., NO_3^- , SO_4^{2-}) largely influence As speciation and
53 partitioning between groundwater and solid phases (O'Day et al., 2004 b; Langner et al., 2012;
54 Stuckey et al., 2015 a; Zhu et al., 2017; Smith et al., 2017).

55 Peat is a heterogeneous mixture of (partly) decayed plant materials that accumulate anaerobically
56 (Naafs et al., 2019). Abundant reactive organic matter provides electrons for the reductive
57 transformation of Fe (oxyhydr)oxides, thereby influencing the behavior of trace elements that are
58 bound onto Fe (oxyhydr)oxides such as As. In the As contaminated aquifers in South and Southeast
59 of Asia, peat formed in Holocene epoch or the last glacial period is widely embedded in the
60 sediments (McArthur et al., 2001; Wang et al., 2018; Wang et al., 2019b). Influence of the buried
61 peat for As mobilization has been extensively discussed in terms of reductive dissolution of Fe(III)
62 (oxyhydr)oxides. On one hand, dissolved organic matter degraded from plants in the peat lenses
63 can be transported to different locations by groundwater flow, stimulate microbial reduction of
64 Fe(III) (oxyhydr)oxides and As(V) reduction and thereby releasing arsenic into groundwater
65 (McArthur et al. 2001, 2004; Anawar et al. 2003; Fendorf et al., 2010). On the other hand, the
66 detrital peat buried in the sediments can serve as a special sink for As. Following the reductive

67 dissolution of Fe(III) (oxyhydr)oxides and As(V) species, mobilized As(III) species can be
68 subsequently sequestered by sulfides, with sulfide arising from reduced organic sulfide in peat or
69 microbial reduction of SO_4^{2-} (Stuckey et al., 2015 b; Wang et al., 2018; Knappová et al., 2019).
70 Furthermore, recent research shows that reactive organic thiol groups formed by incorporating
71 inorganic sulfide into organic carbon can adsorb As in contaminated peatlands, providing another
72 sink for As (Langner et al., 2012, 2013; Wang et al., 2018). Therefore, the influence of peat for As
73 behavior is complex and affected by Fe-C-S coupled mineralization pathways. Understanding the
74 diagenetic process in the peat layers and related As speciation are vital to gain better understanding
75 on the influence of peat sediments in As immobilization in contaminated anoxic environments.

76 Arsenic-Fe sulfides associations are common features in peat layers, and act an important role for
77 As immobilization. Iron sulfides found in the natural sediments mainly include mackinawite
78 (nominally “FeS”), greigite and pyrite (Wilkin and Ford, 2006; Pickard et al., 2017; Knappová et
79 al., 2019). Recent research suggests that Fe sulfides are main As carriers in the detrital peat of As
80 contaminated aquifer in South and Southeast of Asia. For example, arsenic is mainly sequestered
81 in pyrite found in peat from Mekong River Delta and Bangladesh (Lowers et al., 2007; Stuckey et
82 al., 2015 b; Wang et al., 2018). Several studies have been conducted to study the mechanisms of
83 Fe sulfides formation as well as the adsorption/incorporation behavior of As in the laboratory scale
84 (Benning et al., 2000; Bostick and Fendorf, 2003; Blanchard et al., 2007; Kirk et al., 2010; Le et
85 al., 2017). However, the diagenetic formation process in natural settings and
86 adsorption/incorporation mechanisms for As are still not sufficiently understood because Fe
87 sulfides and related As species are difficult to characterize and quantify due to its oxygen-sensitive
88 nature and poorly crystalline properties.

89 Based on the assumption that diagenetic process especially Fe sulfides formation in the peat can
90 influence As partitioning in sediments and groundwater, we separated three peat lenses from the
91 sediments of Hetao Basin, an important inland basin draining Yellow river with As contaminated
92 groundwater. Using these, we seek to (1) define the S and Fe diagenetic minerals in peat lenses,
93 (2) investigate As speciation in both peat sediments and specific Fe sulfides, and (3) evaluate the
94 potential role of peat layers in controlling the toxicity and mobility of As in aquifers. The buried
95 peat in the Hetao Basin formed either by over-flowed flood debris or swamps is analogous to other
96 peat formed in As contaminated aquifers in South and Southeast Asia, therefore the research results
97 can be applicable to comparable subsurface environments.

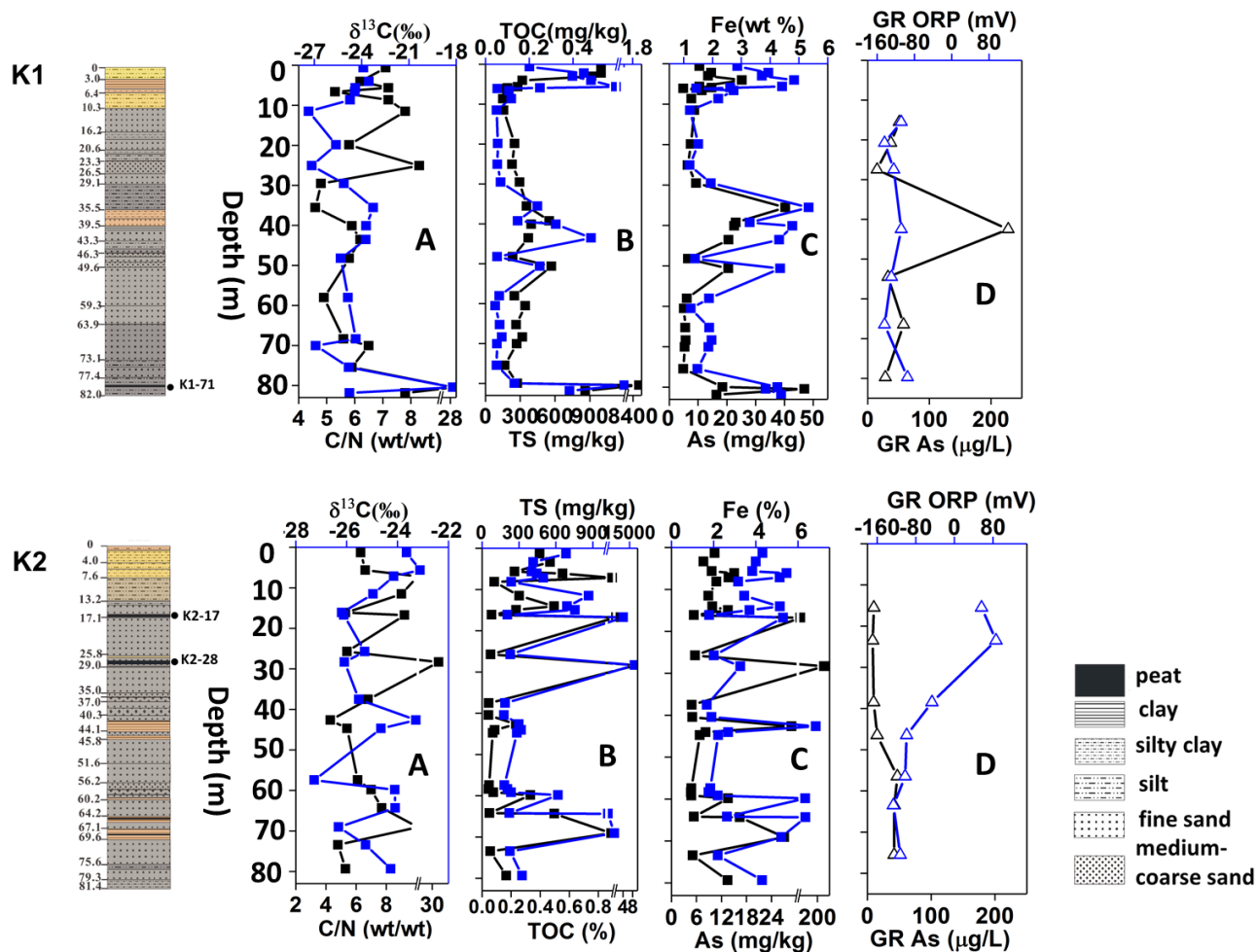
98 **2. Material and Methods**

99 **2.1 Field area**

100 The Hetao Basin is a typical inland basin lying in the central part of Inner Mongolia (China) with
101 the Lang Mountains in the North and the Yellow River in the South, covering an area of about
102 13,000 km². In the early time of late Pleistocene (~120 ka) epoch, the Yellow River began to flow
103 through the Hetao paleolake. At the same time, the paleolake started to shrink due to the cooling
104 climate (Jia et al., 2016). Salt marshes as well as oxbow lakes were generated as a result of
105 paleolake shrinkage and frequent movement of the Yellow River channels (Cai et al., 2019),
106 resulting in the accumulation of organic matter. The study site was located in the flat plain of
107 northwestern Hetao Basin which was one of most As contaminated area. The stratigraphy of the
108 late Pleistocene and the Holocene covered a depth around 150 m, whereas the Holocene sediments
109 primarily included alluvial-fluvial sediments with thicknesses of ~10 m (Deng et al., 2009). Further
110 detailed information about the study area such as hydrological conditions were outlined in a
111 previous study (Zhang et al., 2020).

112 **2.2 Sediments collection, bulk geochemistry composition and mineral phase analysis**

113 Two multilevel wells, K1 (41°0′9.00″N, 106°57′59.20″E) and K2 (41°1′2.10″N,
114 106°57′24.50″E), were selected in the study area. The wells were drilled in October 2015 by the
115 China University of Geosciences (Beijing) (CUGB) using a circulatory drilling method. After
116 bringing the cores to the surface, they were split into 10 cm sections according to lithology and
117 color variations observed visually, and then capped and placed into N₂-purged Mylar bags. More
118 detailed information about well construction and sediments sampling information has been
119 reported by Zhang et al. (2020). Groundwater samples from different depths (sampling length: 1
120 m) were collected after the wells were constructed and then analyzed at CUGB. The geochemical
121 and mineralogical composition of the sediments were analyzed at the Karlsruhe Institute of
122 Technology (KIT). Methods for the groundwater sampling, geochemical analysis, and
123 determination of elemental and organic carbon content and isotopic composition are detailed in
124 the supplementary information (**Supplementary text 1**). Methods for mineralogical
125 characterization of magnetically separated minerals, and sequential extractions of Fe-bearing
126 phases in the bulk sediments are shown in the supplementary information (**Supplementary text 2**
127 **and Supplementary Table S1**). The magnetic susceptibility measurements of the peat sediments
128 are described in detail in **Supplementary text 3**.



129

130 **Fig. 1** Lithology and elemental content in the sediments profiles as well as groundwater redox
 131 conditions and As concentrations from different depths: (A) Isotope signature of organic carbon
 132 ($\delta^{13}\text{C}_{\text{org}}$, blue) and ratio of organic carbon to total nitrogen (C/N, black); (B) total sulfur content
 133 (TS, blue) and total organic carbon (TOC, black); (C) total Fe (blue) and As content (black); and
 134 (D) groundwater redox conditions (GW ORP, blue) and As concentrations (black). Drawing color
 135 of the cores represents the visualized sediments colors, layers labeled with black dots (K1-71, K2-
 136 17, and K2-28) represent the analyzed peat sediments.

137 **2.3 ^{57}Fe Mössbauer analysis**

138 A section of peat was separated from each intact core for Mössbauer analysis at the University of
139 Tübingen. Inside the glovebox (pure nitrogen atmosphere), dried powders of peat samples were
140 loaded into Plexiglas holders (area 1 cm²), forming a thin disc. Samples were kept in airtight jars
141 under anoxic conditions at -20 °C until measurement. Holders were inserted into a closed-cycle
142 exchange gas cryostat (Janis cryogenics) under a backflow of He to minimize exposure to air.
143 Spectra were collected at 20 K using a constant acceleration drive system (WissEL) in transmission
144 mode with a ⁵⁷Co/Rh source. All spectra were calibrated against a 7-µm thick α-⁵⁷Fe foil that was
145 measured at room temperature. Analysis was carried out using Recoil (University of Ottawa) and
146 the Voigt Based Fitting (VBF) routine (Rancourt and Ping, 1991). The half width at half maximum
147 (HWHM) was constrained to 0.13 mm/s during fitting.

148 **2.4 Scanning Electron Microscopy (SEM) and Electron probe microanalysis (EPMA)**

149 Thin sections for SEM imaging and EPMA analysis were prepared at KIT. A section of peat was
150 separated from intact cores, and embedded in an arsenic free-resin in the glovebox after drying
151 (Araldite, 2020). Sections of 1-mm thickness were cut and polished down to a thickness of 80 µm.
152 Thin sections were stored in the glovebox until analysis.

153 Carbon-coated thin sections were used for SEM imaging and EPMA analysis. SEM images were
154 acquired at the GFZ German Research Center for Geosciences using a Zeiss Ultra Plus FE-SEM
155 at an acceleration voltage of 3 kV with 10 µm aperture distance using an In-lens secondary electron
156 detector. Following mineral observations using SEM, selected particles and areas were analyzed
157 at Goethe University by wavelength spectrometer electron probe microanalysis (EPMA, JEOL
158 8900). The operating conditions were 20 keV accelerating voltage and 20 nA beam current. Iron,
159 S, Si, Ca, Mg and As concentrations were quantified using peak counting times of 10 s for Fe, S,
160 Si, Ca, Mg, and 60 s for As. The detection limit for As was about 90 mg/kg. For As, S and Fe

161 mapping, pixel size was set to $0.1 \mu\text{m} \times 0.1 \mu\text{m}$. The analysis volume for particles was
162 approximately $0.2 \mu\text{m} - 0.3 \mu\text{m}$ based on the Monte Carlo simulations.

163 **2.5 As, S and Fe K-edge X-ray absorption spectroscopic analysis**

164 The speciation and local bonding environment of As, S and Fe in selected peat samples were
165 characterized using X-ray absorption spectroscopy (XAS) analysis at the SUL-X beamline at the
166 ANKA synchrotron radiation facility (KIT). Samples were collected from each peat and ground
167 into powder after drying in the glovebox. A sample mass for Fe K-edge XAS analysis was
168 calculated by the program XAFSmass and mixed with boron nitride (Sigma-Aldrich) prior to
169 analysis (Klementiev, 2012). For As and Fe K-edge XAS analysis, powdered samples were
170 suspended in deoxygenated water in the glovebox, drop-casted onto Kapton tape, and sealed using
171 a second piece of Kapton tape. Arsenic K-edge EXAFS spectra for sample K2-28 was analyzed at
172 the BM23 beamline of the European Synchrotron Radiation Facility (ESRF, Grenoble, France)
173 using the same sample preparation method. For S K-edge XAS measurements, dried peat samples
174 were directly loaded onto the Kapton tape surface. Three scans to 12 scans were collected per
175 sample for each As, Fe and S K-edge XAS spectrum. Data reduction and analysis of XAS spectra
176 were performed using Athena software package (Ravel and Newville, 2005). Experimental and
177 data analysis procedures can be found in the supplementary information (**Supplementary text 4**).

178 **3. Results**

179 **3.1 Geochemical composition of peat sediments**

180 Surface sediments (~ 10 m) from cores K1 and K2 were yellowish to brownish in color and fine-
181 grained with a silt/clay like texture, whereas gray aquifer sediments with interbedded brown/gray
182 clay lenses were found at a depth of ~ 10 m (K1) and ~ 14 m (K2) to 82 m (maximum sampled

183 depth) (**Fig. 1**). In borehole K1, a ~5 cm thick black peat band located between 80.4 and 80.5 m
 184 (K1-71) was composed of a poorly sorted mixture of fine sand, clay and small amounts of medium
 185 sand. In borehole K2, a ~5 cm poorly sorted clay peat band was found at a depth of 16.7 - 16.8 m
 186 (K2-17), and a peat layer composed of fine sand and visible detrital plant materials with thickness
 187 of at least of 10 cm was observed at a depth of 28.3 - 28.4 m (K2-28).

188 Arsenic content in the sediments was found to be between 4.7 mg/kg to 40.3 mg/kg (except for the
 189 peat layers) with generally higher content found in clay sediments (**Table 1**). Meanwhile, clay
 190 sediments had slightly higher Fe content (3.94% in average) than silt (2.86% in average) and sand
 191 (1.46 % in average) (**Table 1**). Peat sediments showed significantly higher total organic carbon
 192 (TOC) and total sulfur (TS) content, and C/N ratios than in the underlying and overlying sediments
 193 (**Fig. 1 and Table 1**). Much higher As content was found in the peat lenses (up to ~ 250 mg/kg)
 194 in comparison with other sediments (**Fig. 1 and Table 1**). In comparison with peats K1-71 and
 195 K2-17, peat K2-28 had much higher organic matter as well as total S content (**Table 1**).

196 **Table 1** Geochemical compositions of studied peat sediments and comparison with other
 197 sediments.

Sample name	Depth (m)	As (mg/kg)	Fe (%)	TOC (%)	TS (mg/kg)	C _{org} /N ratio	δ ¹³ C _{org} (‰)
K1-71	~ 80.4	46.9	3.85	1.70	8,836	29.1	-18.2
K2-17	~ 16.7	59.2	5.31	1.33	11,020	9.2	-26.1
K2-28	~ 28.3	256	3.27	9.52	155,970	31.6	-26.1
clay/silty clay	-	18.6 ± 8.9	3.94 ± 0.72	0.40 ± 0.20	365 ± 156	5.9 ± 1.2	-23.7 ± 0.5
silt	-	12.0 ± 5.1	2.86 ± 0.70	0.24 ± 0.14	376 ± 265	7.1 ± 2.4	-24.1 ± 0.5
sand	-	6.0 ± 1.4	1.46 ± 0.26	0.06 ± 0.01	163 ± 67	6.2 ± 1.3	-25.7 ± 0.9

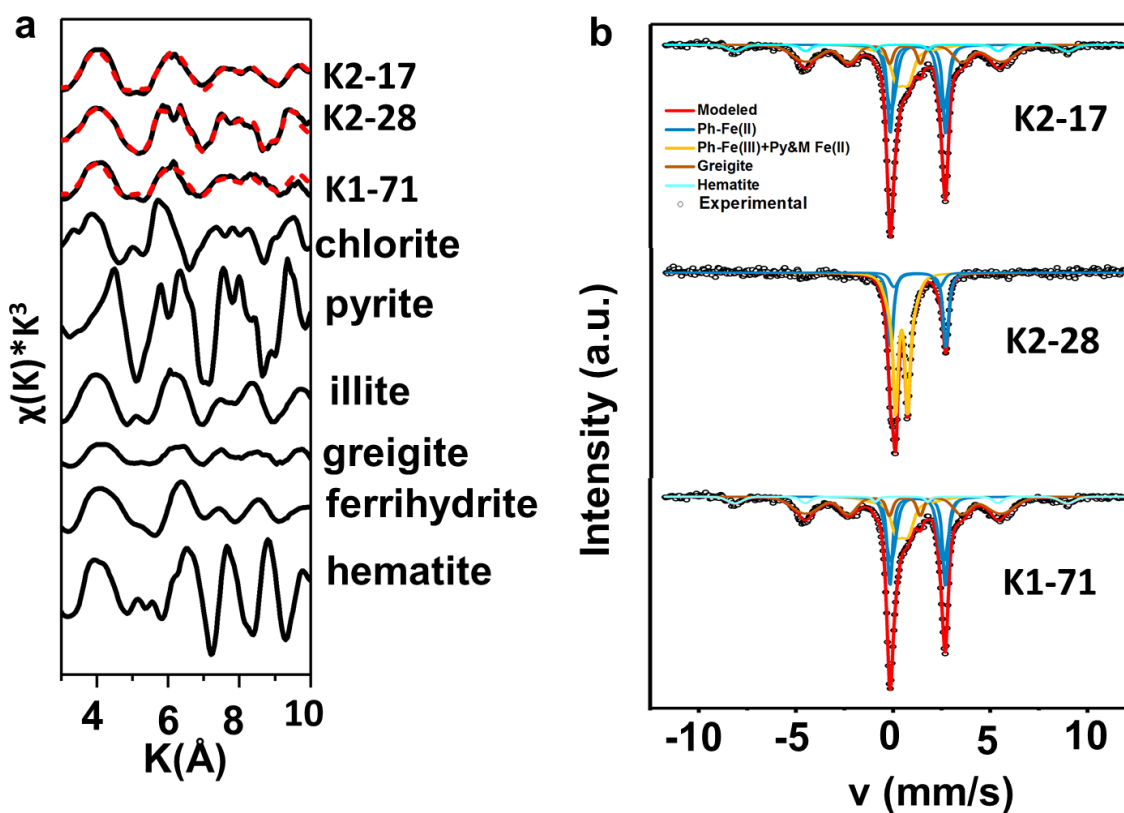
198

199

200 3.2 Fe-containing phases in the peat sediments

201 3.2.1 Fe K-edge XAS and ⁵⁷Fe Mössbauer analysis

202 The pre-edge inflection point near 7112 eV and primary inflection point near 7119 eV in the first
 203 derivative Fe K-edge XANES spectra suggested that Fe sulfides were abundant in the peat lenses
 204 (**Supplementary Fig. S3**) (O'Day et al., 2004 a). The results of Fe K-edge extended X-ray
 205 absorption fine structure (EXAFS) linear combination fitting (LCF) revealed that, aside from
 206 phyllosilicates (~53% and ~66%), greigite (~23% and ~42%) was the primary Fe-bearing mineral
 207 phase in K2-17 and K1-71, respectively. Meanwhile, pyrite (~22%) and ferrihydrite (~17%) in
 208 combination with phyllosilicates (~59%) were the dominant Fe-bearing phases in K2-28 (**Fig. 2 a**
 209 **and Table 2**).



210
 211 **Fig. 2** (a) LCF fitting results of Fe K-edge EXAFS. Black lines represent experimental data for
 212 samples and model compound spectra used for fitting, and red dashed lines represent LCF fits. (b)

213 ⁵⁷Fe Mössbauer spectra collected at 20 K for peat sediments, ph: phyllosilicates; py: pyrite; M:
214 mackinawite.

215 ⁵⁷Fe Mössbauer spectroscopy was used to identify Fe-bearing mineral phases as a complementary
216 technique to synchrotron-based Fe K-edge EXAFS (**Fig. 2 b**). The parameters of the narrow sextet
217 in the peat samples K2-17 and K1-71 were typical of greigite (magnetic hyperfine field of 31.2 T
218 and 32.0 T, isomer shift: 0.59 and 0.57, quadrupole shift of 0.00 and -0.04) (Vandenberghé et al.,
219 1992), comprising ~27% and ~30% of the Fe phases, respectively (**Supplementary Table S6**).
220 Differences less than 10% in the greigite component between the Fe K-edge EXAFS and
221 Mössbauer spectroscopy fits in peat sediments K2-17 and K1-71 is considered to be acceptable
222 (Thomas-Arrigo et al., 2014; Chen et al., 2017).

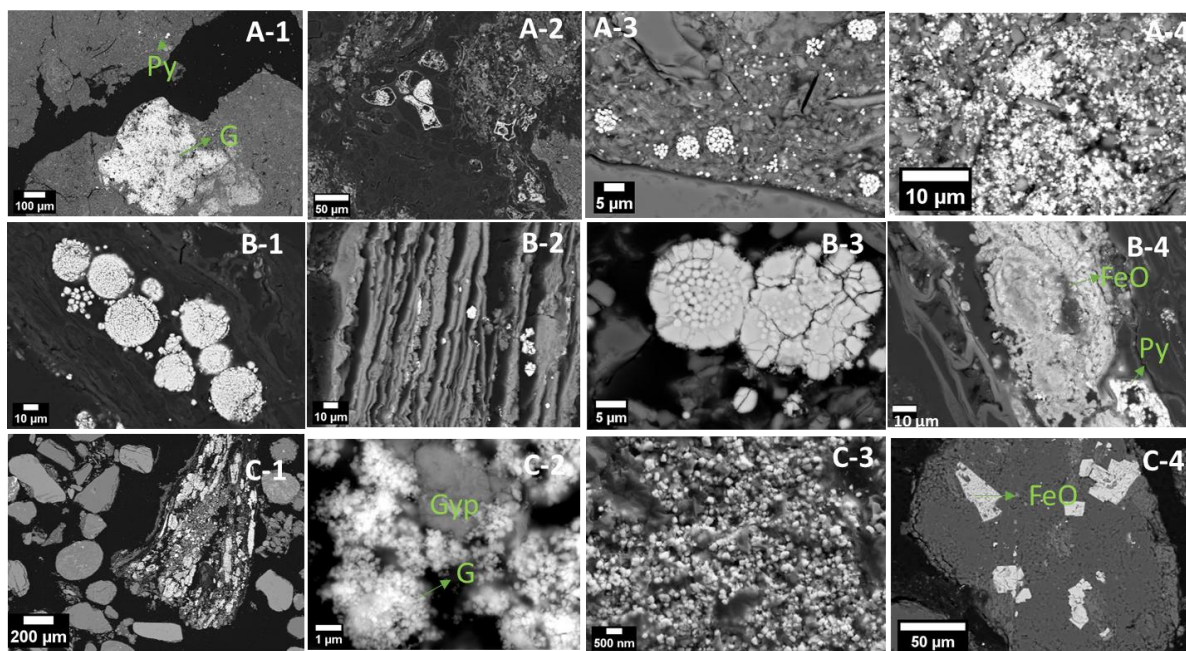
223 Unfortunately, the similarity of phyllosilicates Fe(III) and pyritic Fe(II) in the Mössbauer spectra
224 at 20 K can result to misidentification of pyrite in peat samples K2-17 and K2-28. However, the
225 Fe K-edge EXAFS spectra of pyrite and phyllosilicates can be easily distinguished (O'Day et al.,
226 2004 a), and these fitting results matched the Mössbauer spectroscopy fits (**Table 2 and**
227 **Supplementary Table S6**). Furthermore, an expected ferrihydrite sextet in the 20 K Mössbauer
228 spectra was not observed, even in sample K2-28, while Fe (oxyhydr)oxides were detected by Fe
229 K-edge EXAFS. The magnetic ordering temperature of ferrihydrite is strongly dependent on the
230 mineral purity, crystallite size and crystallinity, and as such the absence of a ferrihydrite sextet in
231 the Mössbauer spectra does not necessarily mean that it is absent, as shown using other
232 spectroscopic measurements (Wang et al., 2016). The presence of ferrihydrite in the K2-28 peat
233 sample was further confirmed by measurements of magnetic susceptibility, which decreased in
234 value from -192 °C to 0 °C (**Supplementary Fig. S2**) (Pannalal et al., 2005).

235 **3.2.2 Texture and morphologies of Fe-bearing phases (SEM-EDX analysis)**

236 The Fe-bearing minerals texture and morphologies were evaluated according to SEM-EDX
237 analysis based on the known minerals which were obtained by Fe K-edge XAS and Fe Mössbauer
238 analysis.

239 Greigite aggregates nucleated in detrital silicates and decaying plant tissues, and less in
240 gypsum/anhydrite (**Fig. 3**). The grain size ranged from ~80 nm to ~500 nm, whereas diverse
241 crystallite habits were observed, including cuboidal, prismatic, and elongated particles.
242 Neoformation of pyrite was also primarily occurred in confined spaces including plant tissues,
243 phyllosilicates grains. The diameters of framboidal pyrites ranged from ~5 μm to ~40 μm (**Fig. 3**).
244 Framboidal crystallites showed either octahedral, cubic (~2 μm in diameter) or spherical crystal
245 habits (~1 μm in diameter). Massive pyrite crystals occurred with octahedral, cubic or irregular
246 habits, with diameters up to ~10 μm . Ferrihydrite was found to be associated with pyrite particles.

247

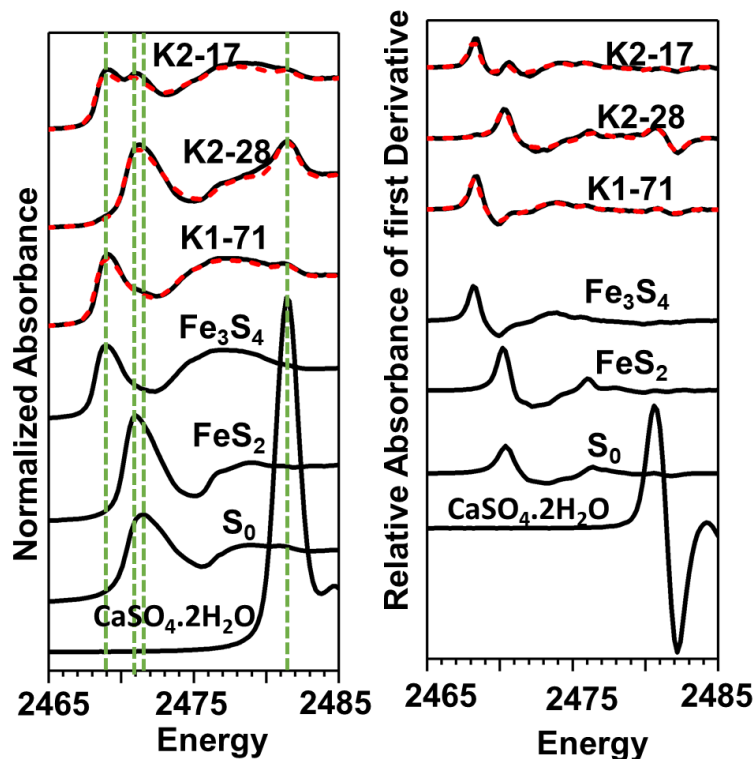


248

249 **Fig. 3** Representative images of peat samples (A) K2-17, (B) K2-28 and (C) K1-71. (A-1)
250 Representative greigite (G) and framboidal pyrite (Py) areas as indicated. (A-2) Greigite/pyrites
251 nucleation in plant cells. (A-3) and (A-4) Nucleation of pyrites/greigite in phyllosilicates. (B-1)
252 Framboidal and massive pyrites nucleation in plant tissues. (B-2) Massive pyrites nucleation in the
253 phyllosilicates. (B-3) Framboidal pyrites nucleation in phyllosilicates. Overgrowth rims and
254 interior crystallites were visible. (B-4) Mixture of ferrihydrite and pyrites in plant tissues/cells. (C-
255 1) Greigite nucleation in phyllosilicates. (C-2) Greigite (G) nucleation in gypsum/anhydrite (Gyp).
256 (C-3) Scattered electron images to show greigite grains. (C-4) Clastic iron oxides (FeO) in the
257 sediment matrix.

258 **3.3 Sulfur speciation in the peat sediments**

259 Sulfur speciation in the peat sediments was analyzed by S K-edge XANES spectra. Based on the
260 primary white line positions, the presence of reduced organosulfur species can be ruled out since
261 they often have white line positions at > 2472 eV (Manceau and Nagy, 2012). The primary
262 inflection points at ~ 2469.1 eV and ~ 2471.1 eV in K2-17 and ~ 2469.1 eV in K1-71 revealed that
263 inorganic sulfides were the primary sulfur-bearing phases, whereas the pronounced inflection
264 points of ~ 2471.2 eV and ~ 2481.6 eV in peat sample K2-28 corresponded to inorganic sulfides
265 and SO_4^{2-} from evaporites, respectively (**Fig. 4**). Iron monosulfide minerals (FeS) were not used
266 in the XANES and XANES first derivative LCF fitting because their characteristic features were
267 not observed in either Fe K-edge XAS analysis or sequential experiments (**Fig. 2 a** and
268 **Supplementary Table S2**). Sulfur K-edge first derivative XANES LCF fitting showed that S^{2-} is
269 the dominant S-bearing phase in K1-71 ($\sim 93\%$) and K2-17 ($\sim 70\%$). In sample K2-28, $\sim 30\%$ and
270 $\sim 60\%$ of S was in the form of S^{-1} and zero-valent sulfur (S_0), respectively (**Fig. 4 and Table 2**).



271
 272 **Fig. 4** Results of LCF fitting for S K-edge XANES and first derivative K-edge XANES spectra.
 273 Black lines represent experimental data, whereas red dashed lines represent the fits. Green dashed
 274 lines represent inflection points of selected model compounds.

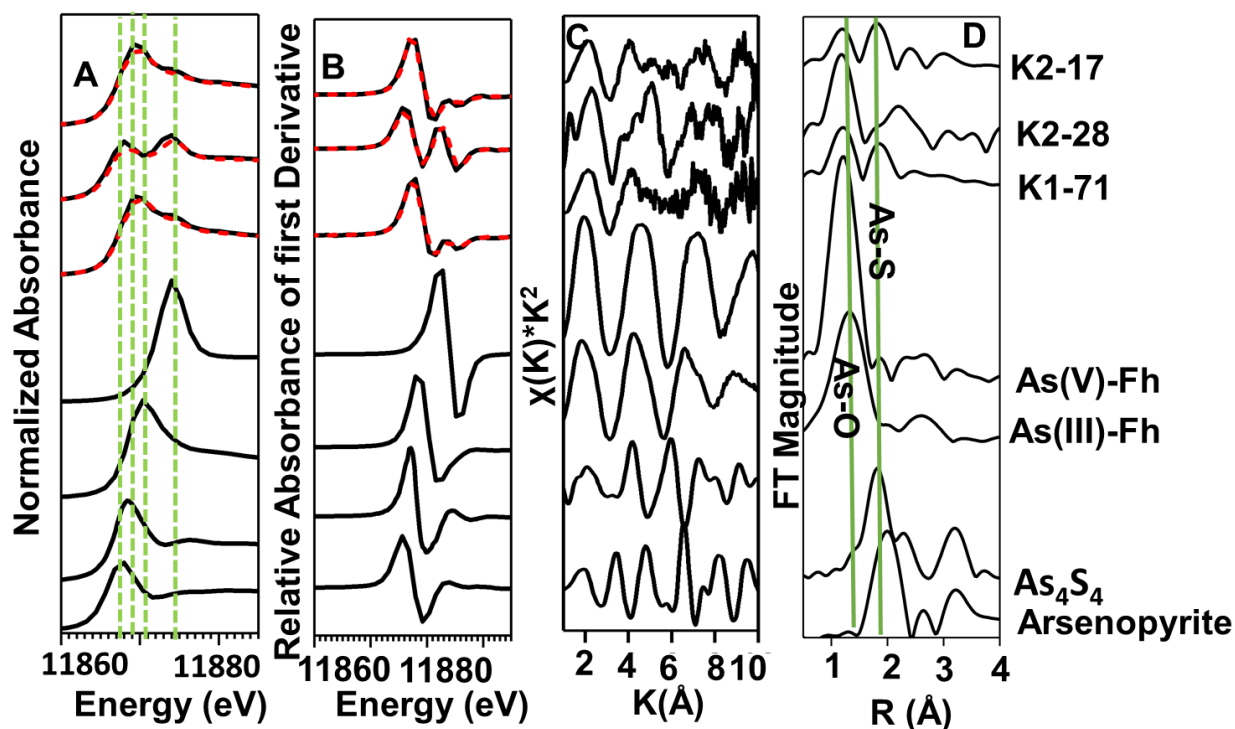
275 3.4 Arsenic speciation and distribution in the peat sediments

276 3.4.1 As K-edge XAS analysis

277 The peat sediments of K1-71 and K2-17 both had white line energies near 11870 eV, which most
 278 likely indicates As(III) species were coordinated by sulfide (Smith et al., 2005). Arsenian
 279 pyrite/arsenopyrite detected in sample K2-17 do not seem to be major sinks for As due to the
 280 absence of the associated white line at ~ 11867.6 eV and the minimal pyrite content ($< 5\%$) (**Fig.**
 281 **5 A and Table 2**). The first shells of the Fourier-transformed EXAFS spectra of K2-17 and K1-
 282 71 were comparable with the As(III)-O bond distance (~ 1.7 Å), while the second shell was
 283 consistent with the As(III)-S bond distance (~ 2.3 Å) (Bostick and Fendorf, 2003) (**Fig. 5 D**). First

284 derivative K-edge XANES LCF fitting shows that ~ 40% of As is in the form of As-sulfide
 285 compounds in K2-17 and K1-71 while around 50% of As is in the form of arsenite (**Table 2**).

286 In peat K2-28, two inflection points occurred at ~11868 eV and ~11874 eV (**Fig. 5 A**), suggesting
 287 that the sample was mainly composed of arsenopyrite/arsenian pyrite (~11868 eV) and arsenate
 288 (~11874 eV). First derivative As K-edge XANES LCF fitting showed that ~61% and ~27% of As
 289 was presented as arsenopyrite/arsenian pyrite and As(V) species, respectively (**Table 2**).



290

291 **Fig. 5** As K-edge (A) XANES and (B) first-derivative XANES spectra of peat sediments and
 292 selected model compounds. The red dashed lines represent fits and the green dashed lines represent
 293 inflection points of selected model compounds (i.e., As(III)/As(V) adsorbed onto ferrihydrite,
 294 realgar (As₄S₄), arsenopyrite). (C) The k^2 weighted $\chi(k)$ EXAFS spectra and their corresponding
 295 Fourier-transformations (D) The green lines represent the As-O and As-S bonding distances.

296

297 **Table 2 Summary of S, Fe and As K-edge XANES or EXAFS LCF fitting results**

Sample	Mineralogical composition (% mol S)						
	XANES first-derivative						
	pyrite	greigite	S ₀	CaSO ₄ ·2H ₂ O	R ²		
K2-17	14 (2.6)	70 (4.1)	15 (3)	1 (0.4)	0.091		
K2-28	30 (2.0)	-	61 (2.9)	9 (0.4)	0.039		
K1-71	-	93 (1.2)	5 (1.1)	2 (0.3)	0.058		
Sample	Mineralogical composition (% mol As)						
	XANES first-derivative						
	realgar	arsenopyrite	As (III)-Fh	As (V)-Fh	R ²		
K2-17	47 (6.9)	0 (4.2)	46 (2.1)	7 (1.5)	0.0245		
K2-28	8(5.0)	61 (6)	3.8 (2.4)	27 (1.7)	0.0516		
K1-71	41 (0.5)	-	50 (1.8)	10 (1.1)	0.0197		
Sample	Mineralogical composition (% mol Fe)						
	EXAFS						
	pyrite	greigite	chlorite	illite	hematite	ferrihydrite	R ²
K2-17	3 (0.8)	23 (2.5)	19 (1.5)	47 (3.9)	8 (0.9)	-	0.0469
K2-28	23 (0.9)	-	39 (1.4)	18 (3.1)	-	21 (6.4)	0.0445
K1-71	-	42 (4.5)	24 (2.8)	29 (3.7)	5 (6.8)	-	0.1581

298

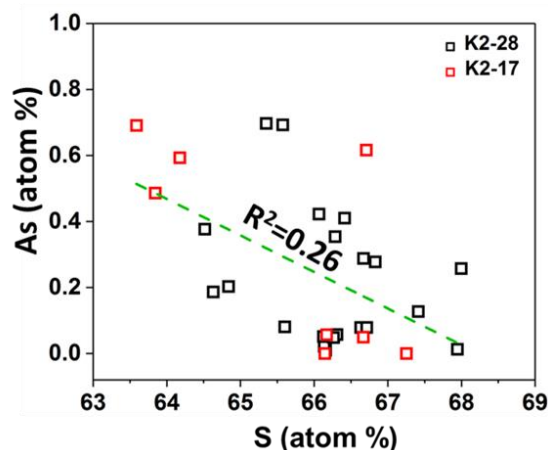
299 **3.4.2 Arsenic content and distribution in pyrite and greigite**

300 Arsenic content of the pyrite and greigite grains was measured by EPMA and summarized in **Table**
301 **3**. Arsenic content in the pyrite grains ranged from < 90 mg/kg (detection limit of EPMA) to
302 ~11,000 mg/kg in both K2-17 and K2-28, respectively. Weak linear least squares fit was obtained
303 for the As:S atomic ratio in the pyrite grains ($R^2 = 0.26$) (**Fig. 6**). Framboidal rims with over-grown
304 pyrite crystallites contained more As than the framboid centers evidenced by two framboid
305 measurements (**Supplementary Table S5**). Arsenic distributions in pyrites were heterogeneous,
306 while the spatial distribution of As fluorescence intensities in the framboids showed a different
307 picture compared to S and Fe (**Fig. 7**). Ferrihydrite aggregates had average As content about 4,000
308 mg/kg, which was comparable with the average As content in pyrite measured using EPMA in
309 peat K2-28 (**Supplementary Table S5**).

310 **Table 3** Arsenic content in pyrite and greigite grains in the peat sediments based on the EPMA
 311 analyses.

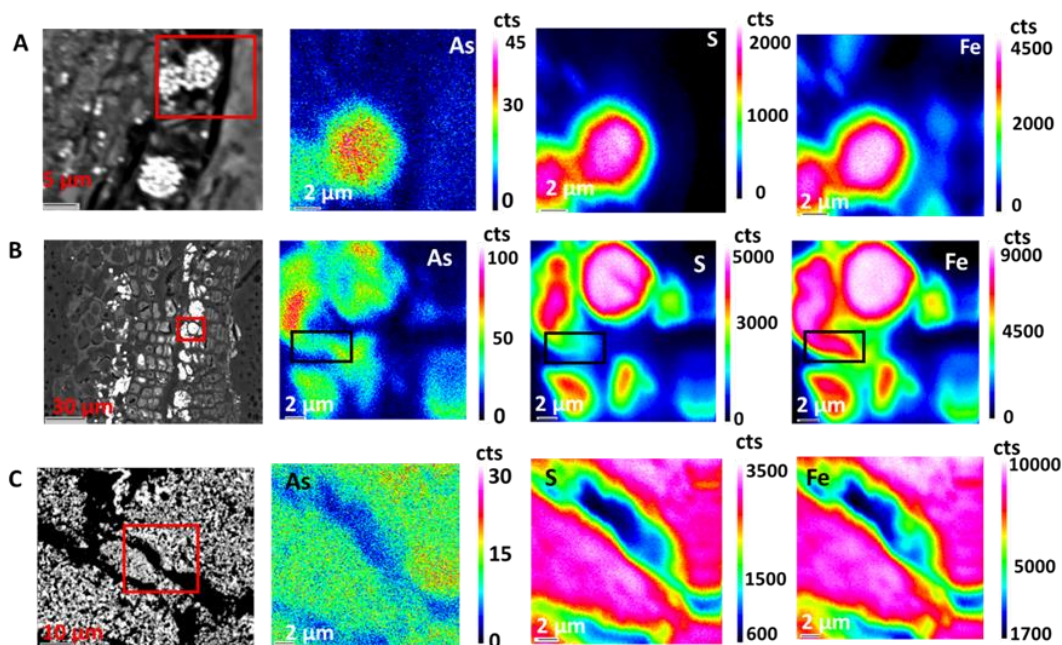
Sample name	Mineral	S/Fe (avg. atomic %)	Min [As] (mg/kg)	Max [As] (mg/kg)	Average [As] ± SD (mg/kg)	n
K2-17	pyrite	2.00	< 90	11,040	5,205 ± 5,155	8
	greigite	1.24	460	1,380	1,024 ± 341	5
K2-28	pyrite	2.00	170	11,450	3,760 ± 3,523	22
K1-71	greigite	1.31	480	1,270	895 ± 321	8

312
 313 In contrast to pyrite, arsenic had a relatively homogeneous distribution in the greigite grains
 314 ranging from 500 to 1,400 mg/kg (**Table 3**). Spatial As distribution was similar to the distribution
 315 of S and Fe fluorescence intensities (**Fig. 7**). Unfortunately, the result obtained from EPMA
 316 analysis may slightly underestimate the As content in the pyrite and greigite, while the total weight
 317 percent of S and Fe is 80% and 93% (on average) for greigite and pyrite, respectively
 318 (**Supplementary Table S5**). Except Fe (oxyhydr)oxides and sulfides, Fe-bearing phyllosilicates,
 319 especially clay minerals such as illite and chlorite, can also incorporate/adsorb As (Fakhreddine et
 320 al., 2015). However, our results showed that the influence from phyllosilicates was limited, as
 321 shown by the S/Fe atom ratios of pyrite and greigite which were similar to the stoichiometric ratios
 322 (**Table 2**). Furthermore, the distribution patterns of elements including Si, Mg and K, which are
 323 the main components of phyllosilicates, do not show any correlations with As distributions
 324 (**Supplementary Fig. S4**).



325

326 **Fig. 6** Sulfur vs As atomic ratio measured by EPMA in peat samples.



327

328 **Fig. 7** Elemental mapping images of S, Fe and As elements obtained by EPMA, mapping area is

329 indicated by red rectangle. (A) Map of framboidal pyrites area in sample K2-17. (B) Map of pyrites

330 area in sample K2-28 which has nucleated in plant tissues, mapping area is indicated by a black

331 rectangle corresponding to ferrihydrite (C) Map of greigite area in sample K1-71.

332 4. Discussion

333 4.1 Diagenetic formation of Fe sulfides

334 The main minerals in the peat sediments include quartz, feldspar, carbonates and clay minerals,

335 which has similar composition with the other sediments in the cores (Wang et al., 2019 a). This

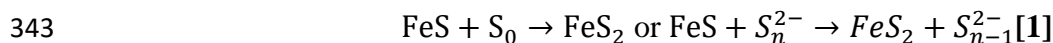
336 suggests that the peat sediments have the same provenance with other sediments. Furthermore, the

337 Fe sulfides found in the peat are likely of authigenic origin which can only be transported via small

338 scales because they are susceptible to oxidation (Lowers et al., 2007). Therefore, the Fe sulfides

339 found in the peat sediments were formed *in situ*.

340 Two proposed mechanisms, which are still under debate, can explain this pyrite formation via
341 mackinawite (nominally “FeS”) transformation, either by “FeS” reacting with
342 polysulfides/elemental sulfur (S₀) (**Eq. 1**) or “FeS” reacting with H₂S (**Eq. 2**) (Benning et al., 2000):



345 Reaction between S₀ precipitates and mackinawite [**eq. 1**] is most likely the dominant mechanism
346 of pyrite formation since large proportions of S₀ (60% of total S) are detected together with pyrite.
347 S₀ could have formed though sulfide oxidation coupled with Fe(III) reduction in such Fe-enriched
348 sediments. Formation of pyrite via the polysulfides/S₀ pathway is typical in the oxic-anoxic
349 transition zone of sediments (Berner, 1970; Neumann et al., 2005; Koeksoy et al., 2019), In the
350 early diagenetic stage, the degradation of organic matter in the saturated water provides electrons
351 for the reductive dissolution of SO₄²⁻ and Fe(III). This is followed by the subsequent precipitation
352 of “FeS” upon saturation of Fe(II) and S(-II), and thereby resulting in the formation of pyrite via
353 “FeS” reacting with S₀. The inhomogeneous framboid and euhedral pyrite sizes distribution could
354 indicate unsteady geochemical conditions (Wilkin et al., 1996, 1997). The overgrowth of framboid,
355 as well as the filled texture, is usually related to the secondary diagenetic growth of pyrite after
356 formation in the surface water-sediment interface during early diagenetic process (Wilkin and
357 Barnes, 1997), and the growth rate is limited by the sulfide supply, which can be constrained by
358 labile organic matter in the sulfidic conditions or availability of SO₄²⁻ in porewater.

359 Greigite is a metastable iron sulfide mineral that is suggested to form as an intermediate during the
360 oxidative transformation of mackinawite to pyrite (Vasiliev et al., 2008; Rickard and Luther, 2007;
361 Pickard et al., 2017). However, the formation pathway and preservation mechanisms of this

362 metastable mineral phase are still not fully understood, even though it has been increasingly
363 recognized as an important sedimentary mineral. There have been few studies that show
364 transformation of mackinawite to pyrite can be inhibited in natural sediments settings (Wilkin and
365 Ford, 2006; Holmkvist et al., 2011; Burton et al., 2011). This is the case in one of the peats (K1-
366 71) from Hetao Basin, wherein greigite is shown in the sample. In comparison with pyrite-
367 dominant peats, greigite-dominant peats have less organic matter and sulfur content, whereas the
368 Fe content is comparable. This can be attributed to the likely precipitation of mackinawite which
369 could remove sulfide from the pore water. The excess Fe^{2+} could exhaust sulfide, therefore,
370 preventing polysulfide/ S_0 formation and the subsequent transformation of greigite to pyrite. The
371 lower sulfide flux in greigite-dominant layers compared to pyrite-dominant layers can be related
372 to the limited labile organic carbon content or lower SO_4^{2-} concentration. This further emphasizes
373 the importance of polysulfides/ S_0 for the transformation of metastable iron sulfide precursors to
374 pyrite under anoxic conditions in natural sediments. However, formation of greigite from a
375 mackinawite precursor also requires an oxidant (Wilkin and Barnes, 1997; Schippers and
376 Jørgensen, 2002; Hunger and Benning 2007). In the surface water-sediment interface, the
377 penetration of oxidants such as O_2 and NO_3^- probably favor the transformation of FeS into greigite
378 while polysulfides/ S_0 is limited.

379 Phyllosilicates and decaying plant tissues provide the ideal micro-environments for pyrite/greigite
380 nucleation and growth. Reactive Fe^{2+} provided by Fe-rich phyllosilicates via chemical or microbial
381 reduction can induce supersaturation and precipitation of mackinawite on the silicates surface and
382 subsequent transformation into pyrite/greigite. Some sulfate reducing bacteria such as
383 *Desulfovibrio sp.* can reduce organic sulfur species into inorganic sulfides, which can also drive
384 mackinawite formation in tissues (Alschuler et al., 1983). In addition, plant tissues can provide

385 active surface area and decrease the oversaturation required for Fe sulfide nucleation (Rickard et
386 al., 2007). Since organic sulfur is not detected in the S K-edge XANES spectra (< 5%) of the peat
387 samples, it suggests that microbial reduction of organic sulfur could have provided the inorganic
388 sulfide needed for the formation of the mackinawite precursor. This result is contrary with previous
389 study which has shown that inorganic sulfide is coupled with organic carbon as thiol functional
390 groups, which in turn can sequester metalloids such as As (Langer et al., 2012; Wang et al., 2018).
391 This might be a result of the differences in the ratio of reactive Fe to sulfur. The high abundance
392 of reactive iron can remove inorganic sulfide in such Fe-rich sediments, thereby inhibiting
393 transformation of inorganic sulfide to thiol functional groups.

394 **4.2 Arsenic incorporation into Fe sulfides**

395 Although relatively weakly correlated, the linear relationship between the S and As atomic ratios
396 suggests that As possibly substitutes for S in the crystal structure of pyrite to form arsenian pyrite.
397 The incorporation of As into pyrites is further evidenced by the As K-edge derivative XANES fits.
398 In the pyrite-dominant peat sediments, our XANES data showed that approximate 60% of As exists
399 as As(-I). The pyrite sequestration mechanism for As is consistent with previous studies of pyritic
400 As sequestration mechanisms in natural sediments at low temperatures (Savage et al., 2000;
401 Lowers et al., 2007). Arsenic content in the pyrite particles is between < 90 mg/kg to 11,000 mg/kg
402 with an average value around 5,000 mg/kg, showing that pyrite plays an important role for As
403 sequestration in peat sediments. The similar maximum pyrite As concentrations in sediments from
404 Bangladesh and the Hetao Basin suggests that the maximum As content incorporated into pyrite
405 grains is around 1 wt.% under typical aquifer conditions (Lowers et al., 2007). The heterogeneous
406 distributions of As in pyrite can be related to pyrite growth rates as well as contact time with
407 porewater. The slightly higher As concentrations found in the framboid over-growth rims as well

408 as massive pyrites could be related to longer crystallization time, leading to enhanced As
409 incorporation from the surrounding pore water into the pyrite structure (Lowers et al., 2007;
410 Neumann et al., 2013). Moreover, the resulting arsenian pyrites are still expected to be able to
411 adsorb pore water As in the form of As(III) or As(V) species, or form As-S precipitates (Bostick
412 and Fendorf, 2003; Qiu et al., 2018). This is consistent with our field observation that As
413 concentration is relatively low in the groundwater with blackish-suspended particles, which likely
414 corresponds to pyrite.

415 To our knowledge, adsorption and/or incorporation of As by greigite in both lab-scale batch
416 reactions and in engineered and natural aquatic environments are still poorly investigated. The
417 average As content of greigite particles as measured by EPMA, when multiplied by the amount of
418 greigite determined in our samples, is comparable to the fraction of As bound in As sulfide
419 (**Supplementary text 5**). Therefore, our results show that greigite is an important sink for As in
420 the peat sediments with relatively lower S and organic carbon content and is primarily coordinated
421 to sulfur within these particles, which is analogous to realgar evidenced by As K-edge XANES
422 fitting. During greigite formation, oxidation of mackinawite coupled with As(III) species reduction
423 may cause the surface precipitation of greigite and realgar. The findings in our study is consistent
424 with the model predictions by Gallegos et al., (2008), where they argued that the formation of
425 greigite is thermodynamically favorable by the reaction of As(III) species and mackinawite.
426 Realgar and orpiment are also potential As carrier phases in the sulfidic sediments (O'Day et al.,
427 2004 a). However, greigite formation also uses up the available sulfide, therefore limiting As
428 sulfides (i.e., realgar, orpiment) formation. Furthermore, it can also be constrained by relatively
429 lower As concentrations in the pore water since As sulfide formation needs high porewater As
430 concentration (O'Day et al., 2004 b; Langner et al., 2012).

431 4.3 Significance of peat sediments for As mobilization process in aquifers

432 Our study clearly shows that Fe sulfides including greigite and pyrite formed in peat lenses could
433 be important As sinks in contaminated aquifers. Sulfide flux controls Fe sulfides formation, while
434 the sulfide flux would be in turn controlled either by labile organic matter in peat or SO_4^{2-} flux in
435 the SO_4^{2-} limited groundwater (Lowers et al., 2007). In comparison to Fe (oxyhydr)oxides, greigite
436 and pyrite are more thermodynamically stable under these sub-oxic conditions. Therefore, As
437 release caused by reductive dissolution of iron (oxyhydr)oxides would not happen in the
438 groundwater, and competitive adsorption between dissolved phosphate and silica and As on the
439 reactive surfaces of Fe sulfides also cannot occur.

440 However, oxidation of arsenian pyrite to ferrihydrite-As(V) species can be ongoing process under
441 slightly oxic conditions, as we have observed in the peat layer K2-28 (**Fig. 1**). Transferring As
442 from surface or structure of arsenian pyrite onto ferrihydrite can temporarily retards the As release,
443 which is supported by the similar average As content found in the ferrihydrite and pyrite as well
444 as low As concentrations ($< 10 \mu\text{g/L}$) in the groundwater (**Fig. 1**). However, ferrihydrite can
445 potentially be reduced under disturbed groundwater redox conditions, which may cause elevated
446 As concentration in the groundwater, since Fe sulfides re-formation is constrained by labile
447 organic carbon. Groundwater redox conditions in draining delta or basins of South and Southeast
448 Asia frequently experience anthropogenic perturbations, as well as seasonal fluctuations (Harvey
449 et al., 2002; Fendorf et al., 2010), making Fe sulfides as an As source with respect to potential As
450 remobilization. In recent years, *in situ* formation of Fe sulfides is suggested to remediate
451 groundwater As pollution (Keimowitz et al., 2007; Pi et al., 2017). However, it is not suggested to
452 apply it in such naturally unmanaged aquifer.

453 Previous studies also suggested that reactive organic carbon can be transported to other area by
454 groundwater flow, therefore stimulating As release following by Fe (oxyhydr)oxides and As(V)
455 species reduction (McArthur et al., 2001,2004; Fendorf et al., 2010), but there is no solid evidence
456 to prove that. Our study indicates that the labile organic matter buried in the peat sediments from
457 aquifer can already be exhausted by early diagenetic Fe and S reduction. Our findings are
458 consistent with the results found by Stuckey et al. (2015b), wherein organic matter leached from
459 Mangrove deposits from Mekong delta cannot be able to simulate Fe (oxyhydr)oxides reduction.

460 **5. Summary and Conclusion**

461 Detrital peat formed from swamps or excessive flood debris is common in the As-contaminated
462 aquifer of South and South-east Asia. To investigate the mineral diagenesis and sequestration
463 behavior for As in these organic carbon-rich deposits, three peat lenses were retrieved from two
464 cores with depths up to 80 m in the Hetao Basin.

465 Simultaneous microbial reduction of organic and inorganic sulfate favored Fe sulfide nucleation
466 in the decaying plant tissues and phyllosilicates. Greigite and pyrite formed in surface water-
467 sediment interface as the diagenetic minerals were stable in peat sediments under anoxic conditions.
468 Excessive Fe(II) compared to sulfide due to lower sulfide flux potentially inhibited pyrite
469 formation in the sulfidic porewater.

470 Peat sediments show a stable sink for As under steady anoxic conditions with As concentrations
471 up to 250 mg/kg. Pyrite crystallites can have As content up to 11,000 mg/kg, with a majority of
472 the As(-I) substitutes for S(-I) in the pyrite structure. Arsenic content in the greigite grains is
473 relatively homogeneous, ranging from ~500 to ~1,400 mg/kg. We suggest that As forms distinct
474 As sulfide precipitates in greigite-rich peats, as indicated by our As K-edge XAS data.

475 Anthropogenic perturbations and seasonal fluctuation of groundwater tables can largely change
476 the groundwater redox conditions, for example, recharge of surface water caused by groundwater
477 extraction infiltrates O₂ into groundwater. The increase of redox potential can induce Fe sulfides
478 (e.g. pyrite and greigite) transfer to Fe (oxyhydr)oxides and temporarily retard As release into
479 groundwater. However, reductive dissolution may in turn release As from the newly-formed iron
480 (oxyhydr)oxide phase, as there is insufficient organic matter for transformation of these phases to
481 Fe sulfide minerals and sequestration of As.

482 **Acknowledgement**

483 XRF, XRD, CSA, as well as HR-ICP-MS and IR-MS analysis were performed at KIT. The authors
484 give thanks to Beate Oetzel, Claudia Moessner and Gesine Preuss for their technical assistance.
485 We thank Ralf Steininger for his support during the collection of Fe, As and S K-edge XAS data
486 at ANKA. The authors also acknowledge the CUGB group for their assistance during the field trip
487 to the Hetao Basin and travel funding provided from the GRACE graduate program at KIT. We
488 are also grateful for the advice from Elisabeth Eiche for C isotope analysis and Nicolas Börsig for
489 XAS fitting analysis. The As K-edge XAS data of K2-28 was collected at the BM23 beamline at
490 ESRF (experiment no. EV-338), and the authors thank Sakura Pascarelli for assistance during
491 beamtime. We further acknowledge the financial support from the Helmholtz Recruiting Initiative
492 (award number I-044-16-01) awarded to L.G.B. J.P.H.P. and A.N.T. are supported by the
493 European Union's Horizon 2020 Marie Skłodowska-Curie Innovative Training Network Grant No.
494 675219, and H.Y.W is supported by Chinese scholarship Council Grant No. 201606400055.
495 Finally, we are grateful for the insightful comments from EIC Prof. Jeffrey Catalano, AE Prof.
496 Caroline Peacock and three anonymous reviewers.

497 **Reference**

498 Altschuler, Z.S., Schnepfe, M.M., Silber, C.C., Simon, F.O. (1983). Sulfur diagenesis in
499 Everglades peat and origin of pyrite in coal. *Science*, **221(4607)**, 221-227.

500 Anawar, H. M., Akai, J., Komaki, K., Terao, H., Yoshioka, T., Ishizuka, T., Safiullah S., Kato, K.
501 (2003). Geochemical occurrence of arsenic in groundwater of Bangladesh: sources and
502 mobilization processes. *J. Geochem. Explor*, **77(2-3)**, 109-131.

503 Benning, L. G., Wilkin, R. T., Barnes, H. L. (2000). Reaction pathways in the Fe–S system below
504 100 °C. *Chem. Geol*, **167(1-2)**, 25-51.

505 Berner, R.A., (1970). Sedimentary pyrite formation. *Am. J. Sci*, **268(1)**, 1-23.

506 Blanchard, M., Alfredsson, M., Brodholt, J., Wright, K., Catlow, C. R. A. (2007). Arsenic
507 incorporation into FeS₂ pyrite and its influence on dissolution: a DFT study. *Geochim. Cosmochim.*
508 *Acta*, **71(3)**, 624-630.

509 Bostick, B.C., Fendorf, S. (2003). Arsenite sorption on troilite (FeS) and pyrite (FeS₂). *Geochim.*
510 *Cosmochim. Acta*, **67(5)**, 909-921.

511 Burton, E. D., Johnston, S. G., Bush, R. T. (2011). Microbial sulfidogenesis in ferrihydrite-rich
512 environments: Effects on iron mineralogy and arsenic mobility. *Geochim. Cosmochim. Acta*,
513 **75(11)**, 3072-3087.

514 Cai, M., Ye, P., Yang, X., Li, C. (2019). Vegetation and climate change in the Hetao Basin
515 (Northern China) during the last interglacial-glacial cycle. *J. Asian. Earth. Sci*, **171**, 1-8.

516 Chen, C., Kukkadapu, R.K., Lazareva, O., Sparks, D.L. (2017). Solid-phase Fe speciation along
517 the vertical redox gradients in floodplains using XAS and Mössbauer spectroscopies. *Environ. Sci.*
518 *Technol*, **51(14)**, 7903-7912.

519 Deng, Y., Wang, Y., Ma, T. (2009). Isotope and minor element geochemistry of high arsenic
520 groundwater from Hangjinhouqi, the Hetao Plain, Inner Mongolia. *Appl. Geochem*, **24(4)**, 587-
521 599.

522 Fakhreddine S, Dittmar J, Phipps D, et al. (2015). Geochemical Triggers of Arsenic Mobilization
523 during Managed Aquifer Recharge. *Environ. Sci. Technol*, **49(13)**:7802-7809.

524 Fendorf, S., Michael, H. A., van Geen, A. (2010). Spatial and temporal variations of groundwater
525 arsenic in South and Southeast Asia. *Science*, **328(5982)**, 1123-1127.

526 Gallegos, T. J., Han, Y. S., Hayes, K. F. (2008). Model predictions of realgar precipitation by
527 reaction of As (III) with synthetic mackinawite under anoxic conditions. *Environ. Sci. Technol*,
528 **42(24)**, 9338-9343.

529 Guo, H., Liu, C., Lu, H., Wanty, R. B., Wang, J., Zhou, Y. (2013). Pathways of coupled arsenic
530 and iron cycling in high arsenic groundwater of the Hetao basin, Inner Mongolia, China: An iron
531 isotope approach. *Geochim. Cosmochim. Acta*, **112**, 130-145.

532 Harvey, C. F., Swartz, C. H., Badruzzaman, A. B. M., Keon-Blute, N., Yu, W., Ali, M. A., Jay J.,
533 Beckie R., Niedan V., Brabander D., Oates P. M., Ashfaque K. N., Islam S., Hemond H. F., Ahmed
534 M. F. (2002). Arsenic mobility and groundwater extraction in Bangladesh. *Sci.*, **298(5598)**, 1602-
535 1606.

536 Holmkvist, L., Ferdelman T. G., Jørgensen B. B. (2011). A cryptic sulfur cycle driven by iron in
537 the methane zone of marine sediment (Aarhus Bay, Denmark). *Geochim. Cosmochim. Acta*, 3581-
538 3599.

539 Hunger, S., Benning, L. G. (2007). Greigite: a true intermediate on the polysulfide pathway to
540 pyrite. *Geochem. Trans*, **8(1)**, 1.

541 Islam, F. S., Gault, A. G., Boothman, C., Polya, D. A., Charnock, J. M., Chatterjee, D., Lloyd, J.
542 R. (2004). Role of metal-reducing bacteria in arsenic release from Bengal delta sediments. *Nature*,
543 **430(6995)**, 68.

544 Jia, L., Zhang, X., Ye, P., Zhao, X., He, Z., He, X., Zhou, Q., Li, J., Ye, M., Wang, Z., Meng, J.
545 (2016). Development of the alluvial and lacustrine terraces on the northern margin of the Hetao
546 Basin, Inner Mongolia, China: Implications for the evolution of the Yellow River in the Hetao area
547 since the late Pleistocene. *Geomorphol*, **263**, 87-98.

548 Keimowitz, A. R., Mailloux, B. J., Cole, P., Stute, M., Simpson, H. J., Chillrud, S. N. (2007).
549 Laboratory investigations of enhanced sulfate reduction as a groundwater arsenic remediation
550 strategy. *Environ. Sci. & technol*, **41(19)**, 6718-6724.

551 Kirk, M. F., Roden, E. E., Crossey, L. J., Brealey, A. J., Spilde, M. N. (2010). Experimental
552 analysis of arsenic precipitation during microbial sulfate and iron reduction in model aquifer
553 sediment reactors. *Geochim. Cosmochim. Acta*, **74(9)**, 2538-2555.

554 Klementiev, K. V. (2012). XAFS_{mass}. A program for calculating the mass of XAFS samples.

555 Knappová, M., Drahota, P., Falteisek, L., Culka, A., Penížek, V., Trubač, J., Mihaljevič M.,
556 Matoušek, T. (2019). Microbial sulfidogenesis of arsenic in naturally contaminated wetland soil.
557 *Geochim. Cosmochim. Acta*, **267**, 33-50.

558 Kocar, B.D., Borch, T., Fendorf, S. (2010). Arsenic repartitioning during biogenic sulfidization
559 and transformation of ferrihydrite. *Geochim. Cosmochim. Acta*, **74(3)**, 980-994.

560 Koeksoy, E., Sundman, A., Byrne, J.M., Lohmayer, R., Planer-Friedrich, B., Halevy, I., Konhauser,
561 K.O., Kappler, A. (2019). Formation of green rust and elemental sulfur in an analogue for
562 oxygenated ferro-euxinic transition zones of Precambrian oceans. *Geology*, **47(3)**, 211-214.

563 Langner, P., Mikutta, C., Kretzschmar, R. (2012). Arsenic sequestration by organic sulphur in peat.
564 *Nat. Geosci*, **5(1)**, 66.

565 Langner, P., Mikutta, C., Suess, E., Marcus, M. A., Kretzschmar, R. (2013). Spatial distribution
566 and speciation of arsenic in peat studied with microfocussed X-ray fluorescence spectrometry and
567 X-ray absorption spectroscopy. *Environ. Sci. Technol*, **47(17)**, 9706-9714.

568 Le, P. P., Blanchard, M., Brest, J., Boulliard, J. C., Ikogou, M., Stetten, L., Wang, S., Landort G.,
569 Morin, G. (2017). Arsenic Incorporation in Pyrite at Ambient Temperature at Both Tetrahedral SI
570 and Octahedral FeII Sites: Evidence from EXAFS-DFT Analysis. *Environ. Sci. Technol.*, **51(1)**,
571 150-158.

572 Lowers, H. A., Breit, G. N., Foster, A. L., Whitney, J., Yount, J., Uddin, M. N., Muneem, A. A.
573 (2007). Arsenic incorporation into authigenic pyrite, Bengal Basin sediment, Bangladesh.
574 *Geochim. Cosmochim. Acta*, **71(11)**, 2699-2717.

575 Manceau, A. and Nagy, K.L. (2012). Quantitative analysis of sulfur functional groups in natural
576 organic matter by XANES spectroscopy. *Geochim. Cosmochim. Acta*, **99**, 206-223.

577 McArthur, J. M., Banerjee, D. M., Hudson-Edwards, K. A., Mishra, R., Purohit, R., Ravenscroft,
578 P., Cronin A., Howarth R. J., Chatterjee A, Talukder T., Lowry, D., Houghton S., Chadha D.K
579 (2004). Natural organic matter in sedimentary basins and its relation to arsenic in anoxic ground
580 water: the example of West Bengal and its worldwide implications. *Appl Geochem*, **19(8)**, 1255-
581 1293.

582 McArthur, J. M., Ravenscroft, P., Safiulla, S., Thirlwall, M. F. (2001). Arsenic in groundwater:
583 testing pollution mechanisms for sedimentary aquifers in Bangladesh. *Water Resour. Res.*, **37(1)**,
584 109-117.

585 Naafs, B. D. A., Inglis, G. N., Blewett, J., McClymont E. L., Lauretano V., Xie, S., Evershed, R.
586 P., Pancost, R. D. (2019). The potential of biomarker proxies to trace climate, vegetation, and
587 biogeochemical processes in peat: A review. *Glob Planet Change*, **179**, 57-79.

588 Neumann, T., Rausch, N., Leipe, T., Dellwig, O., Berner, Z., Böttcher, M.E. (2005). Intense pyrite
589 formation under low-sulfate conditions in the Achterwasser lagoon, SW Baltic Sea. *Geochim.*
590 *Cosmochim. Acta*, **69(14)**, 3619-3630.

591 Nickson, R., McArthur, J., Burgess, W., Ahmed, K. M., Ravenscroft, P., Rahmanī, M. (1998).
592 Arsenic poisoning of Bangladesh groundwater. *Nature*, **395(6700)**, 338.

593 O'Day, P.A., Rivera Jr, N., Root, R., Carroll, S.A., (2004 a). X-ray absorption spectroscopic study
594 of Fe reference compounds for the analysis of natural sediments. *Am. Mineral.*, **89(4)**, 572-585.

595 O'Day, P. A., Vlassopoulos, D., Root, R., Rivera, N. (2004 b). The influence of sulfur and iron on
596 dissolved arsenic concentrations in the shallow subsurface under changing redox conditions. *Proc.*
597 *Natl. Acad. Sci.*, **101(38)**, 13703-13708.

598 Pannalal, S.J., Crowe, S.A., Cioppa, M.T., Symons, D.T., Sturm, A. and Fowle, D.A. (2005).
599 Room-temperature magnetic properties of ferrihydrite: A potential magnetic remanence carrier?
600 *Earth Planet. Sci. Lett.*, **236(3-4)**, 856-870.

601 Pi, K., Wang, Y., Xie, X., Ma, T., Liu, Y., Su, C., Zhu, Y., Wang, Z. (2017). Remediation of
602 arsenic-contaminated groundwater by in-situ stimulating biogenic precipitation of iron sulfides.
603 *Water Res.*, **109**, 337-346.

604 Pickard D., Mussmann M., Steadman J. A. (2017). Sedimentary Sulfides. *Elements*, **13**(2), 117-
605 122.

606 Qiu, G., Gao, T., Hong, J., Luo, Y., Liu, L., Tan, W., Liu, F. (2018). Mechanisms of interaction
607 between arsenian pyrite and aqueous arsenite under anoxic and oxic conditions. *Geochim.*
608 *Cosmochim. Acta*, **228**, 205-219.

609 Rancourt, D.G., Ping, J.Y. (1991). Voigt-based methods for arbitrary-shape static hyperfine
610 parameter distributions in Mössbauer spectroscopy. *Nucl. Instrum. Methods Phys. Res: Beam*
611 *Interactions with Materials and Atoms*, **58**(1), 85-97.

612 Ravel, B. and Newville, M.A.T.H.E.N.A. (2005). ATHENA, ARTEMIS, HEPHAESTUS: data
613 analysis for X-ray absorption spectroscopy using IFEFFIT. *J. Synchrotron Radiat*, **12**(4), 537-541.

614 Rickard D. and Luther G. W (2007). Chemistry of Iron Sulfides. *Chem. Rev.*, **107**(2), 514-562.

615 Rickard, D., Grimes, S., Butler, I., Oldroyd, A. and Davies, K.L. (2007). Botanical constraints on
616 pyrite formation. *Chem. Geol.*, **236**(3-4), 228-246.

617 Savage, K.S., Tingle, T.N., O'Day, P.A., Waychunas, G.A. and Bird, D.K. (2000). Arsenic
618 speciation in pyrite and secondary weathering phases, Mother Lode gold district, Tuolumne
619 County, California. *Appl. Geochem.*, **15**(8), 1219-1244.

620 Schippers, A., Jørgensen, B.B. (2002). Biogeochemistry of pyrite and iron sulfide oxidation in
621 marine sediments. *Geochim. Cosmochim. Acta*, **66**(1), 85-92.

622 Smith, P.G., Koch, I., Gordon, R.A., Mandoli, D.F., Chapman, B.D., Reimer, K.J. (2005). X-ray
623 absorption near-edge structure analysis of arsenic species for application to biological
624 environmental samples. *Environ. Sci. Technol.*, **39**(1), 248-254.

625 Smith, R. L., Kent, D. B., Repert, D. A., Böhlke, J. K. (2017). Anoxic nitrate reduction coupled
626 with iron oxidation and attenuation of dissolved arsenic and phosphate in a sand and gravel aquifer.
627 *Geochim. Cosmochim. Acta*, **196**, 102-120.

628 Stuckey, J. W., Schaefer, M. V., Benner, S. G., Fendorf, S. (2015 a). Reactivity and speciation of
629 mineral-associated arsenic in seasonal and permanent wetlands of the Mekong Delta. *Geochim.*
630 *Cosmochim. Acta*, **171**, 143-155.

631 Stuckey, J. W., Schaefer, M. V., Kocar, B. D., Dittmar, J., Pacheco, J. L., Benner, S. G., Fendorf,
632 S. (2015 b). Peat formation concentrates arsenic within sediment deposits of the Mekong Delta.
633 *Geochim. Cosmochim. Acta*, **149**, 190-205.

634 Thomas-Arrigo, L.K., Mikutta, C., Byrne, J., Barmettler, K., Kappler, A., Kretzschmar, R. (2014).
635 Iron and arsenic speciation and distribution in organic flocs from streambeds of an arsenic-
636 enriched peatland. *Environ. Sci. Technol.*, **48**(22), 13218-13228.

637 Upadhyaya, G., Jackson, J., Clancy, T. M., Hyun, S. P., Brown, J., Hayes, K. F., Raskin, L. (2010).
638 Simultaneous removal of nitrate and arsenic from drinking water sources utilizing a fixed-bed
639 bioreactor system. *Water Res.*, **44**(17), 4958-4969.

640 Vandenberghe, R.E., De Grave, E., De Bakker, P.M.A., Krs, M. and Hus, J.J. (1992). Mössbauer
641 effect study of natural greigite. *Hyperfine Interact*, **68(1-4)**, 319-322.

642 Vasiliev, I., Franke, C., Meeldijk, J. D., Dekkers, M. J., Langereis, C. G., Krijgsman, W. (2008).
643 Putative greigite magnetofossils from the Pliocene epoch. *Nat. Geosci*, **1(11)**, 782.

644 Wang, H. Y., Guo, H. M., Xiu, W., Bauer, J., Sun, G. X., Tang, X. H., Norra, S. (2019 a).
645 Indications that weathering of evaporite minerals affects groundwater salinity and As mobilization
646 in aquifers of the northwestern Hetao Basin, China. *Appl. Geochem*, **109**, 104416.

647 Wang, X., Zhu, M., Koopal, L.K., Li, W., Xu, W., Liu, F., Zhang, J., Liu, Q., Feng, X., Sparks,
648 D.L. (2016). Effects of crystallite size on the structure and magnetism of ferrihydrite. *Environ. Sci.:*
649 *Nano*, **3(1)**, 190-202.

650 Wang, Y., Le Pape, P., Morin, G., Asta, M. P., King, G., Bártoová, B., Suvorova, E., Frutschi, M.,
651 Ikgou, M., Cong Pham V.H., Le Vo, P., Herman, F., Charlet, L., Bernier-Latmani B., (2018).
652 Arsenic speciation in Mekong Delta sediments depends on their depositional environment.
653 *Environ. Sci. Technol*, **52(6)**, 3431-3439.

654 Wang, Y., Pi, K., Fendorf, S., Deng, Y., Xie, X. (2019 b). Sedimentogenesis and
655 hydrobiogeochemistry of high arsenic Late Pleistocene-Holocene aquifer systems. *Earth-Sci. Rev*,
656 **189**, 79-98.

657 Wilkin, R. T., Arthur, M. A., Dean, W. E. (1997). History of water-column anoxia in the Black
658 Sea indicated by pyrite framboid size distributions. *Earth Planet. Sci. Lett*, **148(3-4)**, 517-525.

659 Wilkin, R. T., Barnes, H. L., Brantley, S. L. (1996). The size distribution of framboidal pyrite in
660 modern sediments: an indicator of redox conditions. *Geochim. Cosmochim. Acta*, **60(20)**, 3897-
661 3912.

662 Wilkin, R. T., Ford, R. G. (2006). Arsenic solid-phase partitioning in reducing sediments of a
663 contaminated wetland. *Chem. Geol*, **228(1-3)**, 156-174.

664 Wilkin, R.T. and Barnes, H.L. (1997). Formation processes of framboidal pyrite. *Geochim.*
665 *Cosmochim. Acta*, **61(2)**, 323-339.

666 Winkel, L., Berg, M., Amini, M., Hug, S. J., Johnson, C. A. (2008). Predicting groundwater arsenic
667 contamination in Southeast Asia from surface parameters. *Nat. Geosci*, **1(8)**, 536.

668 Wolthers, M., Charlet, L., van Der Weijden, C.H., Van der Linde, P.R., Rickard, D. (2005).
669 Arsenic mobility in the ambient sulfidic environment: Sorption of arsenic (V) and arsenic (III)
670 onto disordered mackinawite. *Geochim. Cosmochim. Acta*, **69(14)**, 3483-3492.

671 Zhang, Z., Guo, H. M., Liu, S., Weng, H. C., Han, S. B., Gao, Z. P. (2020). Mechanisms of
672 groundwater arsenic variations induced by extraction in the western Hetao Basin, Inner Mongolia,
673 China. *J. Hydrol*, **583(124599)**, 1-13.

674 Zhu, Y. G., Xue, X. M., Kappler, A., Rosen, B. P., Meharg, A. A. (2017). Linking genes to
675 microbial biogeochemical cycling: lessons from arsenic. *Environ. Sci. Technol*, **51(13)**, 7326-7339.